Aust. J. Phys., 1989, **42**, 289–306

Neutron Kikuchi Effect and Practical Problems Associated with Its Observation

S. L. Town,[A] *T. F. Smith*[B] *and M. M. Elcombe*[C]

[A] Advanced Electronic Materials Group, School of Physics, University of N.S.W., Kensington, N.S.W. 2033, Australia.
[B] Department of Physics, Monash University, Clayton, Vic. 3168, Australia.
[C] Australian Nuclear Science and Technology Organisation, Lucas Heights Research Laboratories, Private Mail Bag 1, Menai, N.S.W. 2234, Australia.

Abstract

The theory of the neutron Kikuchi effect has been re-examined and an exact formulation in reciprocal space derived. The conditions necessary for its observation have been considered and appropriate data from a lead single crystal have been collected on the triple-axis spectrometer at the HIFAR reactor in the laboratories of the Australian Nuclear Science and Technology Organisation. A series of constant-$\boldsymbol{Q}$ phonon scans across the predicted positions of the Kikuchi lines show reductions in the integrated phonon intensity, which appear to move as expected with changes in the scattered neutron wavevector.

1. Introduction

The Kikuchi effect arises from the secondary Bragg scattering of diffuse inelastic radiation generated in a crystal. The effect was first observed by Kikuchi (1928) using a beam of electrons passing through mica plates of varying thicknesses. The diffraction pattern he observed consisted of black and white lines appearing in pairs, which have since become known as Kikuchi lines. The possibility of observing the effect using X-rays was considered by Friedrich *et al.* (1912) when they were devising an X-ray diffraction experiment, although the effect was actually observed much later by Geisler *et al.* (1948) and Grenville-Wells (1951).

The potential for using the Kikuchi effect with the sample crystal both as scatterer and analyser has been demonstrated for X-rays by Bushuev *et al.* (1983). The effect has been invoked (Wilkins *et al.* 1983) to explain sharp dips (Ti *et al.* 1983; Kashiwase *et al.* 1982) observed in non-resonant Mössbauer measurements of TDS profiles. There appears to be only one reported instance of a neutron TDS profile exhibiting a dip (Graf *et al.* 1981). However, although the authors drew a comparison with the similar γ-ray dips, they cautioned against attaching any physical significance to the observation.

Wilkins (1983) has discussed in detail the geometrical aspects of the neutron Kikuchi effect and the possibility of observing it using the standard diffraction geometry. More recently Petrascheck (1985) has considered the distribution of intensity across a neutron Kikuchi line as a function of angle for a perfect crystal.

0004-9506/89/030289$03.00

For thermal neutrons the significant energy change that occurs on scattering by wavevector $\boldsymbol{q}$ from a phonon complicates the scattering geometry in that the incident ($\boldsymbol{k}_0$) and scattered ($\boldsymbol{k}_s$) wavevectors do not terminate on the same Ewald sphere. In his derivations for the equation of the Kikuchi loci, Wilkins (1983) made the physically reasonable approximation that $k_0 - k_s \ll k_0$, i.e. $q \ll k_0$ and proceeded to formulate the K-loci in terms of instrumental space coordinates $\Delta 2\theta, \Delta\omega$ where $\Delta 2\theta$ and $\Delta\omega$ are, respectively, the detector and crystal settings relative to the exact Bragg condition. The calculated Kikuchi loci are then a pair of straight lines, corresponding to phonon creation and annihilation, the slopes of which are discontinuous at the origin (Wilkins 1983).

In Section 2 of this paper the experimental conditions necessary to observe the Kikuchi effect with neutrons are discussed. Following this the theory is reformulated in reciprocal space such that it is in a form which is appropriate for the described experiment. This leads to reciprocal and real space coordinates for the K-lines without any approximations. Finally we present some experimental results from lead which are consistent with the observation of the neutron Kikuchi effect.

2. Experimental Considerations

Various criteria were considered in planning an experiment to observe the Kikuchi effect. For the effect to occur two processes must take place within the crystal; the creation or annihilation of a phonon and a self-analysing Bragg reflection.

The usual technique for the observation of the Kikuchi effect employs a photographic film to record the dark–bright contrast lines from a slightly misoriented crystal. This requires intense radiation sources and very good angular resolution. Neutron sources are inherently large and diffuse and the efficiency of neutron film methods is very low, making film detection a non-viable option.

Strategies for observation using a neutron counting system are different from those employing films. To obtain adequate intensity requires both a high neutron flux and a large sample volume. At the same time, sufficient angular and energy resolution must be achieved to observe the effect. The angular resolution is achieved by using Soller collimators, which destroy the real space resolution, while maintaining reciprocal space resolution. The energy resolution is achieved by using a high monochromator scattering angle $2\theta_m$.

The effect should be observable on a standard four-circle diffractometer. However, the instruments at the Lucas Heights Research Laboratories do not have Soller collimators and the incoming energy resolution is too poor. A limited series of measurements were made on the diffractometer D10, at the ILL, Grenoble, but the results were inconclusive. It was therefore decided to search for the Kikuchi effect using the triple-axis spectrometer. The advantages here were:

(1) The phonon part of the two-stage process could be guaranteed by using the constant-$\boldsymbol{Q}$ technique, where $\boldsymbol{Q}$ is the scattering vector, $\boldsymbol{q}+\boldsymbol{G}_\omega$ ($\boldsymbol{G}_\omega$ is the Bragg reciprocal lattice vector at crystal rotation $\Delta\omega$ and $\boldsymbol{q}$ is the phonon wavevector). By selecting $\boldsymbol{Q}$ values at and close to those

at which the Kikuchi effect is predicted to occur, the phonon intensity could be used as a probe for the secondary Bragg scattering.

(2) A high neutron flux over a large area was available at the sample position.

(3) The large beam area enabled a large sample to be used. This increased the intensity of inelastic scattering and also enhanced the fraction of scattered intensity elastically scattered out of the scattered beam.

Achieving the required resolution presented a problem. The triple-axis spectrometer at the Lucas Heights Research Laboratories, while having a good neutron flux and low background level, is only a medium resolution instrument. Both the monochromator and analyser crystals have mosaic widths of the order of 0·8°. The primary beam has 1·0° full width at half maximum (FWHM). The collimation before the sample was 0·5° (FWHM) and 0·62° (FWHM) before the analyser. The detector has an acceptance angle of 3°. The measured widths of the resolution function (with analyser collimation of 1·25°) parallel and perpendicular to $\boldsymbol{G}_\omega(q_\lambda, q_\omega)$ are 0·051 and 0·052 Å^{-1} respectively.

Ideally, the instrumental resolution should match the estimated angular spread of the Kikuchi line. The major contributions from the crystal to the width of the line are the mosaic spread and variation of the relevant elastic constant with direction in reciprocal space (Section 3). Depending on the experimental conditions the second term may vary from larger than the first to zero. Thus, an instrumental resolution matched to the sample mosaic is desirable.

Phonon resonances were measured at a series of wavevectors across the predicted Kikuchi line positions with the expectation of observing a reduction in the integrated intensity of the neutron groups when self-energy analysis (secondary Bragg scattering) occurred in the crystal. To make full use of the constant-$\boldsymbol{Q}$ technique, it was decided to reformulate the theory in reciprocal space coordinates.

3. Theory

The scattering geometry for the secondary Bragg scattering of an inelastically scattered neutron is shown in Fig. 1*a* for reciprocal lattice vector $\boldsymbol{G}_\omega$ and phonon wavevector $\boldsymbol{q}$. The scattering diagram is appropriate to the geometry of the triple-axis spectrometer at the Lucas Heights Research Laboratories. The two large circles correspond to the Ewald spheres for $\boldsymbol{k}_0$ and $\boldsymbol{k}_s$, the incident and scattered neutron wavevectors respectively. The small circle at the origin represents a constant energy surface for an acoustic phonon of wavevector $\boldsymbol{q}$. Axes that are parallel and perpendicular to the direction $\boldsymbol{k}'_s$ are convenient for the formulation of the theory and these are denoted by $q_\parallel$ and $q_\perp$ respectively. These axes, which are shown in Fig. 1*b*, are displaced by a rigid rotation of $90-\theta_B^s$ from the conventional axes corresponding to wavelength spread (q_λ) and crystal rotation (q_ω) used by Wilkins (1983) (see the Appendix). Note also that the (q_λ, q_ω) axes here are rigidly fixed in reciprocal space and rotate with the crystal, whereas Wilkins kept these axes fixed relative to the ($\Delta 2\theta, \Delta\omega$) coordinate system. This introduces a rotational displacement of $\Delta\omega$ between the two (q_λ, q_ω) systems. Here θ_B^s is the Bragg angle for the scattered wavevector.

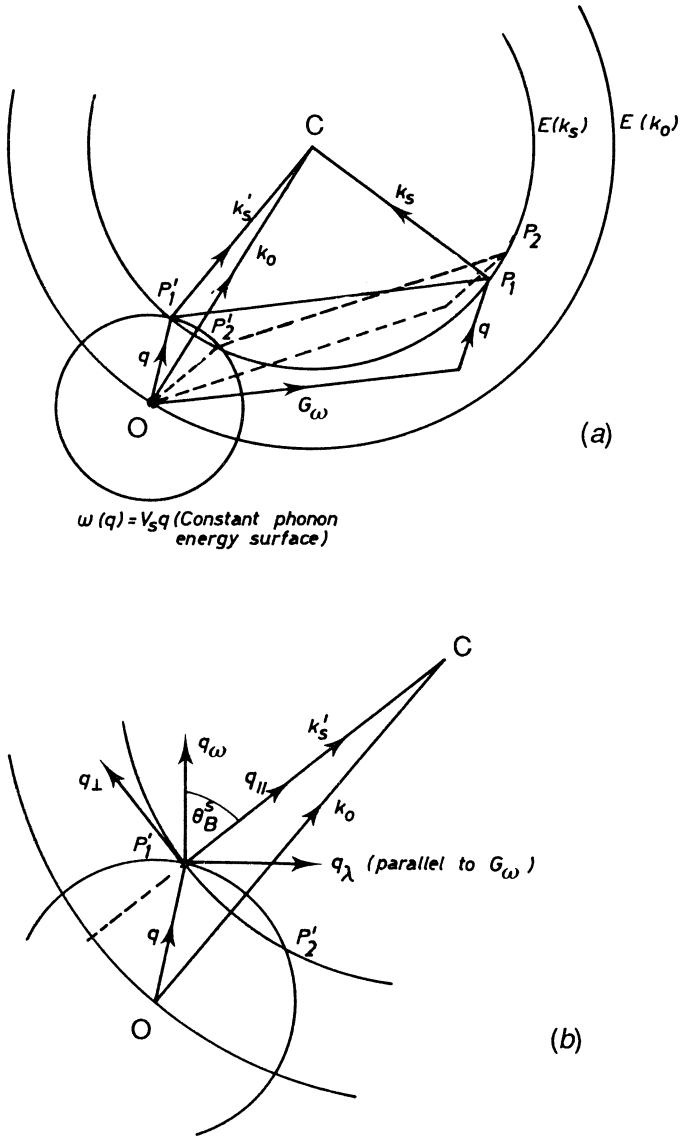

Fig. 1. (*a*) Scattering geometry in reciprocal space for the secondary Bragg scattering of an inelastically scattered neutron, where $E(k_0)$ and $E(k_s)$ represent the Ewald spheres for k_0 and k_s respectively, and $\omega(\boldsymbol{q}) = v_s(\boldsymbol{q})\boldsymbol{q}$ is the constant phonon energy surface. (*b*) Detailed wavevector geometry.

For the point P_1 to lie on a Kikuchi locus requires that in addition to satisfying the conservation of energy condition,

$$\hbar^2(\boldsymbol{k}_0^2 - \boldsymbol{k}_s^2)/2m_n = \epsilon\hbar\omega(\boldsymbol{q}), \tag{1}$$

and the conservation of momentum condition,

$$\boldsymbol{k}_0 = \boldsymbol{k}_s + \boldsymbol{q} + \boldsymbol{G}_\omega, \tag{2}$$

$\boldsymbol{k}_s$ must also satisfy the Bragg condition corresponding to the reciprocal lattice vector $\boldsymbol{G}_\omega$ [m_n is the neutron mass, $\omega(\boldsymbol{q})$ is the phonon frequency for the wavevector $\boldsymbol{q}$ and $\epsilon = 1$ for phonon creation and -1 for phonon annihilation]. Thus, the reciprocal lattice vector $\boldsymbol{G}_\omega$ must necessarily be a spanning vector for the Ewald sphere inscribed by the scattered wavevector. By utilising this condition, the scattering geometry to satisfy all necessary conditions may be embodied in the triangle $OP_1'C$ (Fig. 1*b*), P_1' and P_1 being equivalent points as they are separated by a reciprocal lattice vector. It then remains to solve for the coordinates $q_\parallel^K, q_\perp^K$ of P_1'. From triangle $OP_1'C$, it may readily be shown that

$$\frac{q_\parallel^K}{k_s} = \frac{k_0^2 - k_s^2 - q^2}{2k_s^2}. \tag{3}$$

When combined with the conservation of energy condition (1) this yields the relationships

$$\frac{q_\parallel^K}{k_s} = \epsilon\beta'(\boldsymbol{q})\frac{q}{k_s} - \frac{q^2}{2k_s^2}, \qquad \frac{q_\perp^K}{k_s} = \pm\frac{1}{k_s}(q^2 - q_\parallel^{K2})^{\frac{1}{2}}, \tag{4a, b}$$

for the Kikuchi loci positions, where $\beta' = v_s(\boldsymbol{q})/v_n'$ is the ratio of the velocity of sound in the crystal in the direction of $\boldsymbol{q}$ to the velocity of the scattered neutron. The only approximation in deriving equations (4) is the absence of dispersion, i.e. the phonon frequency $\omega(\boldsymbol{q}) = v_s(\boldsymbol{q})\boldsymbol{q}$.

Several points follow from equations (4):

(1) Both solutions for $q_\perp^K$ are physically significant, corresponding to the two points of intersection P_1' and P_2' in the scattering plane between the constant phonon energy surface and the Ewald sphere for the scattered wavevector. (There is a rotation of the $q_\parallel, q_\perp$ axis frame between the two solutions.)

(2) Although the diagram in Fig. 1 is for phonon creation ($k_0 > k_s$, $\epsilon = 1$ and hence $q_\parallel^K > 0$) equation (4a) with $\epsilon = -1$ gives the K-locus for phonon annihilation ($k_0 < k_s$ and hence $q_\parallel^K < 0$). This locus is continuous with the phonon creation locus through $\boldsymbol{q} = 0$. Thus two pairs of Kikuchi lines corresponding to phonon annihilation and creation are predicted.

(3) Even if $\beta'(\boldsymbol{q})$ is constant with angle, the K-loci are curves. However, for small $\Delta 2\theta, \Delta\omega$ the K-lines are indistinguishable from the straight lines calculated by Wilkins (1983) and are equal in the limit that $\Delta 2\theta, \Delta\omega \to 0$ (see the Appendix for details).

(4) The position of the Kikuchi line varies with the neutron wavevectors used during the measurement, predominantly through the variation of $\beta'(\boldsymbol{q})$ with $\boldsymbol{k}_s$. This variation is a stringent test of the observation of the Kikuchi line.

(5) The condition $|q_\parallel^K| \le |q|$ from equation (4a) implies $\beta'(\boldsymbol{q}) \le (1 \pm q/2k_s)$ for $\epsilon = \pm 1$ (cf. $\beta \le 1$, where $\beta = \beta' k_s/k_0$, Wilkins 1983).

(6) Because the velocity of sound, and hence $\beta'(\boldsymbol{q})$, varies with direction, successive iterations of equations (4) are required to calculate the K-loci.

For a given direction $\boldsymbol{q}$, the elastic constants $C_j(\boldsymbol{q})$ and polarisation vectors $\boldsymbol{e}_j(\boldsymbol{q})$ are obtained from the equations

$$\rho\omega^2(\boldsymbol{q})u_\alpha = 4\pi^2 \sum_\beta \left(\sum_{\gamma\lambda} C_{\alpha\gamma,\beta\lambda}\, q_\gamma\, q_\lambda \right) u_\beta \tag{5}$$

by diagonalisation. Here $C_{\alpha\gamma,\beta\lambda}$ are the elastic constants of the material, $\boldsymbol{u}$ is the displacement vector, $\alpha\beta\gamma\lambda$ are summation indices over x,y,z and $j = 1,2,3$ is a polarisation index (Born and Huang 1954). The calculated variation of the velocity of sound v_s with direction for the transverse acoustic branch polarised in the $1\bar{1}0$ plane in lead is shown in Fig. 2. The elastic constants were taken from Waldorf and Alers (1962).

In addition to the above scattering process, whereby a phonon is created and Bragg scattering of the outgoing $\boldsymbol{k}_s$ beam occurs (k_s Kikuchi line) it is also possible for the incident $\boldsymbol{k}_0$ beam to be Bragg scattered before the phonon $\boldsymbol{q}$ is generated from the same point. In this case P_1' will no longer lie on the Ewald sphere $E(k_s)$. The scattering geometry for this has been omitted from Fig. 1*a* to avoid confusion. In this case, defining the axes $q_{\parallel}, q_{\perp}$ parallel and perpendicular to $\boldsymbol{k}_0'$, the scattered incident wavevector equivalent to $\boldsymbol{k}_s'$, the theory becomes equivalent to that for the k_s Kikuchi effect. The k_0 Kikuchi line positions $(q_{\parallel}^{K}/k_0, q_{\perp}^{K}/k_0)$ are then given by equations (4), with the sign of the quadratic term reversed in (4a), k_0 replacing k_s and $\beta(\boldsymbol{q}) = v_s(\boldsymbol{q})/v_n$ replacing $\beta'(\boldsymbol{q})$, where v_n is the velocity of the incident neutron.

Fig. 3 illustrates the predicted k_s and k_0 Kikuchi lines for k_s values of $2\cdot90$ and $2\cdot65$ Å^{-1} with $\epsilon = 1$ and $q_{\perp} > 0$ in the positive quadrant at $22\bar{2}$ in lead. Corresponding lines for $\epsilon = -1, q_{\perp} < 0$ and $\epsilon = -1, q_{\parallel} > 0, q_{\parallel} < 0$ occur in the other three quadrants.

Bragg scattering for $\boldsymbol{k}_0$ and $\boldsymbol{k}_s$ may occur for other reciprocal lattice points which lie on the respective $E(k_0)$ and $E(k_s)$ Ewald spheres. The identification of these points is most readily achieved by numerically calculating the distance of a reciprocal lattice point from either of these spheres for given points in $(\omega, \boldsymbol{Q})$ space with fixed $\boldsymbol{k}_s$. When this distance is zero the reciprocal lattice point is on the sphere and a Bragg reflection is possible. These points produce loci in $(\omega, \boldsymbol{Q})$ space that are shown in Fig. 4, for points close to $22\bar{2}$ in lead for $k_s = 2\cdot85$ Å^{-1}. The thick curve is the calculated frequency for the transverse acoustic phonon branch derived from the elastic constant data (Fig. 2). The k_s Kikuchi or k_0 Kikuchi condition occurs whenever the locus of a Bragg point for $\boldsymbol{k}_s$ or $\boldsymbol{k}_0$ crosses the phonon curve. The analytical solution points corresponding to the K-loci are included in this method and the intersection positions derived from Fig. 4 are in agreement with the numerical calculation (Table 1). Once a particular lattice point has been identified as fulfilling the Kikuchi condition, the locus of its movement in reciprocal space may be readily calculated from equations (4).

The positions of all these loci vary with the scattered wavevector $\boldsymbol{k}_s$. Fig. 5 shows the calculated positions for the incident and scattered beam K-lines as a function of $\boldsymbol{k}_s$ (again close to $22\bar{2}$ in lead).

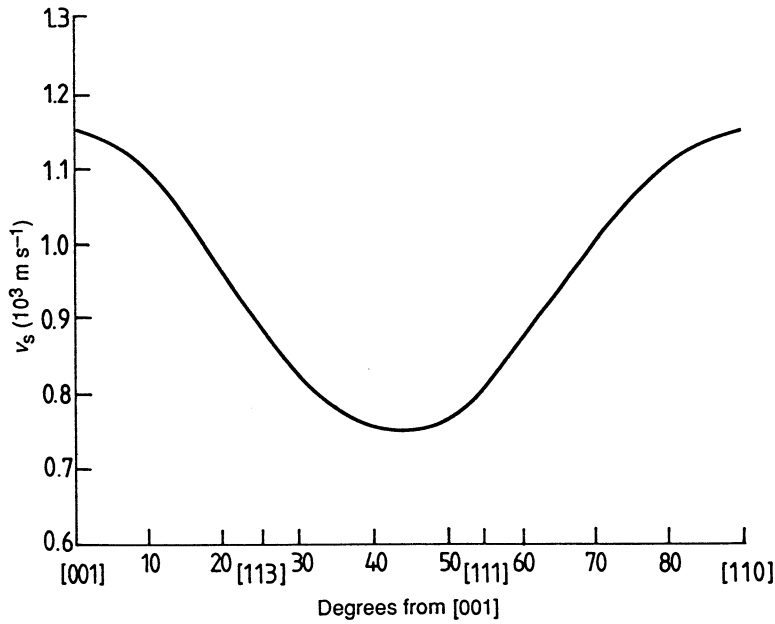

Fig. 2. Variation of the velocity of sound with angle from [001] for the transverse acoustic mode of lead polarised in the $1\bar{1}0$ plane at room temperature.

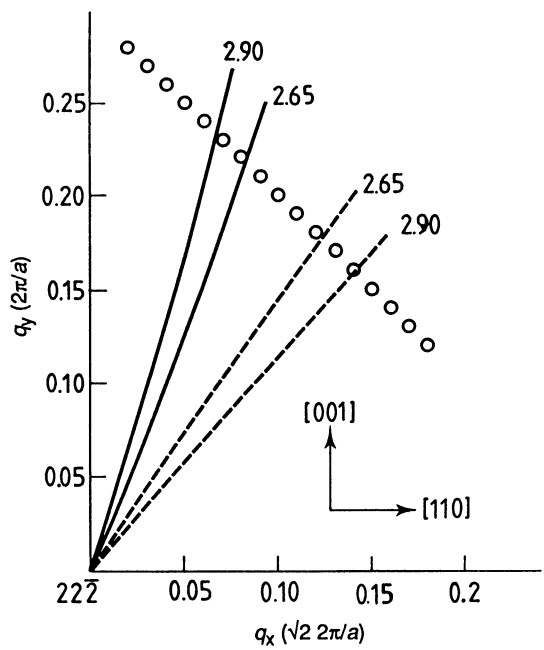

Fig. 3. Reciprocal space map around $(22\bar{2})$ for lead showing some predicted Kikuchi line positions for $k_s = 2\cdot90$ and $2\cdot65$ Å^{-1} and the location of phonon scans (circles). The solid and dashed lines represent k_s and k_0 lines respectively.

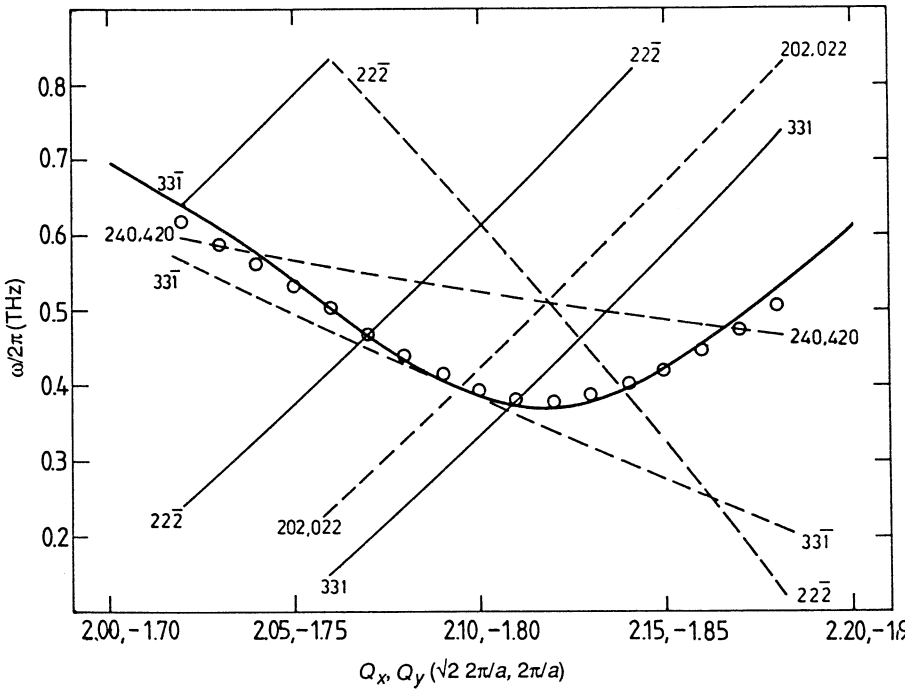

Fig. 4. Loci in $(\omega, \boldsymbol{Q})$ space of possible Bragg reflections from the k_s (solid lines) and k_0 (dashed lines) Ewald spheres (shown for $k_s = 2 \cdot 85$ Å^{-1}) for points close to $(22\bar{2})$ in lead. Also shown by the thick curve is the appropriate phonon frequency for the transverse acoustic mode polarised in the $1\bar{1}0$ plane. Intersections of this curve with the solid and dashed lines are possible k_s and k_0 Kikuchi loci respectively. The data points are the measured phonon frequencies ω_f, for $k_s = 2 \cdot 75$ Å^{-1}.

Table 1. Calculaterd k_s and k_0 Kikuchi line positions for $22\bar{2}$ in lead at the constant scattered neutron wavevectors indicated (for $q_\perp^K > 0$)

Q_x, Q_y are the components of the scattering vector along [110] and [001] respectively

k_s (Å^{-1})	Scattered k_s K-lines Q_x ($\sqrt{2}\,2\pi/a$)	Q_y ($2\pi/a$)	Incident k_0 K-lines Q_x ($\sqrt{2}\,2\pi/a$)	Q_y ($2\pi/a$)
2·65	2·083	−1·783	2·124	−1·824
2·75	2·078	−1·778	2·131	−1·831
2·825	2·072	−1·772	2·137	−1·837
2·86	2·070	−1·770	2·140	−1·840
2·88	2·068	−1·768	2·142	−1·842
2·9	2·067	−1·767	2·144	−1·844
2·92	2·066	−1·766	2·145	−1·845

4. Experiment

Lead was selected as a suitable material on which to try and observe the Kikuchi effect. It has very low elastic constants, which ensures that the condition $\beta' \leq (1 \pm q/2k_s)$ could be satisfied for the low $\boldsymbol{k}_s$ values to obtain

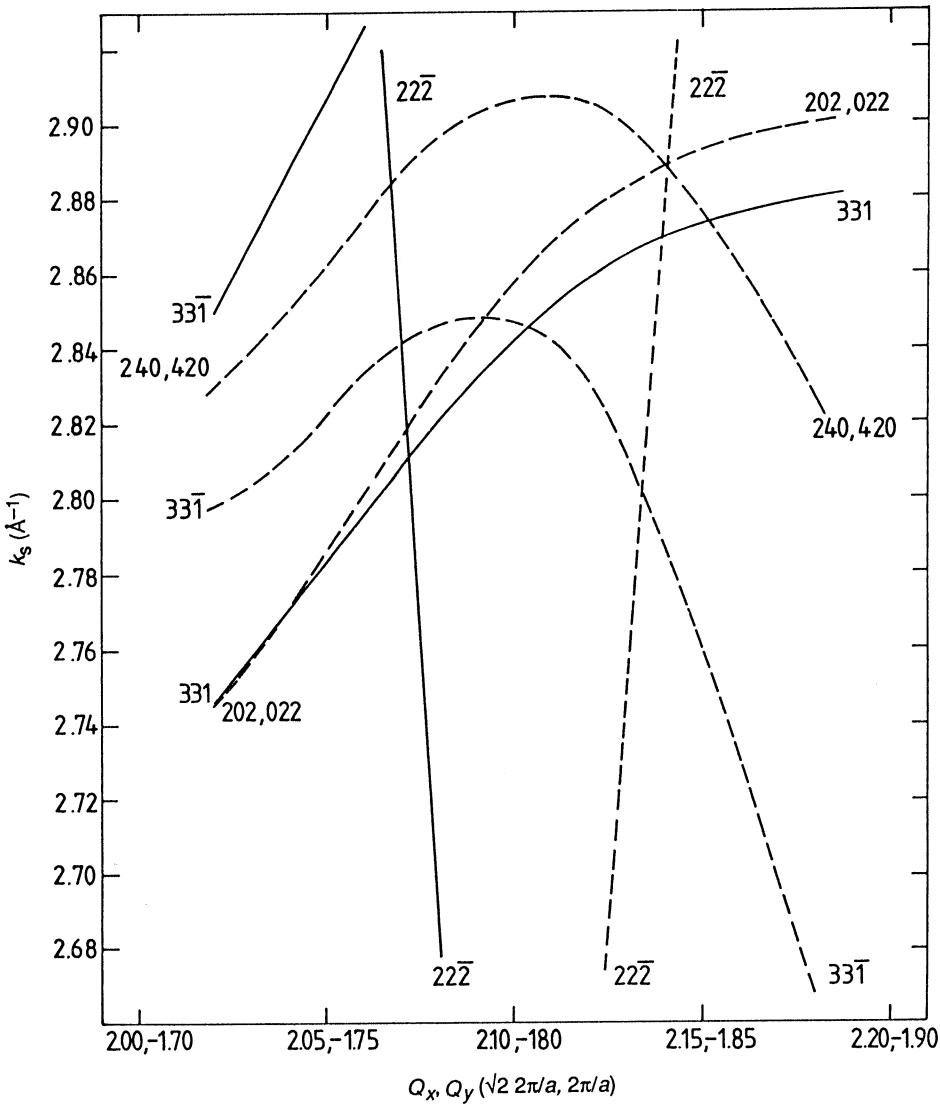

Fig. 5. Variation of predicted Kikuchi loci with k_s along the line of the experimental wavevectors $\boldsymbol{Q}$. The solid and dashed lines distinguish k_s and k_0 Kikuchi loci respectively.

the necessary energy resolution. It has a high coherent scattering length (for good phonon intensity) and has a low neutron absorption cross section so that a large crystal can be used. An old monochromator crystal, 50×27×8 mm^3 with a mosaic spread of 0·6°, compatible with the angular resolution of the instrument, was used. It was mounted with $[1\bar{1}0]$ vertical.

Incident wavelength selection on the triple-axis spectrometer was determined by Bragg reflection from the (111) planes of a single crystal of copper. Scattered wavelength selection was obtained by using the (0004) reflection from a pyrolytic graphite crystal. The monochromator scattering angle ($2\theta_m$) was 58–68° for the

range of wavevectors used, ensuring that good neutron groups, well separated from the incoherent elastic background, were obtained.

The intensity of a phonon resonance is given by the coherent scattering cross section

$$\frac{d^2\sigma}{d\Omega\, dE'} = \frac{\sigma_{coh}}{4\pi}\frac{k_s}{k_0}\frac{(2\pi)^3}{V_0}\frac{1}{2M}\exp(-2W)\sum_{\boldsymbol{q}j}\frac{\{\boldsymbol{Q}\cdot\boldsymbol{e}_j(\boldsymbol{q})\}^2}{\omega_j(\boldsymbol{q})}$$

$$\times\begin{cases}\langle n_{\boldsymbol{q}j}+1\rangle\delta(\omega-\omega_j(\boldsymbol{q}))\delta(\boldsymbol{Q}-\boldsymbol{q}-\boldsymbol{\tau}) & \text{(6a)}\\ \langle n_{\boldsymbol{q}j}\rangle\delta(\omega+\omega_j(\boldsymbol{q}))\delta(\boldsymbol{Q}+\boldsymbol{q}-\boldsymbol{\tau}), & \text{(6b)}\end{cases}$$

where (6a) and (6b) are for phonon creation and annihilation respectively, and the symbols are conventional.

All the phonon scans were done at constant $\boldsymbol{Q}$, maintaining $\boldsymbol{k}_s$ constant, and detector counts were recorded for a preset number of incident neutrons monitored with a ^{235}U fission counter (efficiency $1/v_n$). This allowed intensities to be compared directly.

The terms $\exp(-2W)$ (the Debye–Waller factor), $\langle n_{\boldsymbol{q}j}+1\rangle = \{\exp(\hbar\omega_j(\boldsymbol{q})/kT-1\}^{-1}+1$ (the Bose–Einstein factor for phonon creation) and $\{\boldsymbol{Q}\cdot\boldsymbol{e}_j(\boldsymbol{q})\}^2/\omega_j(\boldsymbol{q})$ all vary with wavevector $\boldsymbol{Q}$. They have been calculated and applied as a correction to the observed intensities.

While the $\boldsymbol{Q}\cdot\boldsymbol{e}(\boldsymbol{q})$ term controls the intensity of the phonon scattering involved in the Kikuchi process, the shape of an observed phonon resonance is controlled by the relative orientation of the phonon dispersion surface and the instrumental resolution function. Sharp resonances are obtained when the long axis of the resolution ellipsoid [in the $(\omega, Q_\perp)$ plane] aligns closely with the phonon dispersion surface. Both these conditions were easily satisfied for the transverse acoustic phonon branch.

In deciding at which Bragg point to measure the transverse acoustic phonon, both the intensity term, $n_{\boldsymbol{q}j}\,\omega_j(\boldsymbol{q})$, and the calculated positions of the k_s and k_0 Kikuchi lines were considered. From Fig. 2, maximum intensity will occur for $\boldsymbol{q}$ at ~45° from the [001] and [110] axes where v_s is a minimum, i.e. close to the ⟨113⟩ and ⟨222⟩ directions. At all such points in the $[1\bar{1}0]$ plane the calculated positions of the k_s and k_0 Kikuchi lines are about 15° (depending on $\boldsymbol{k}_s$) on either side of the $q_\perp(\equiv q_\omega)$ axis. General K-lines were not calculated at this stage. Trial measurements were made around (220), (222) and $(22\bar{2})$ and, as the latter looked most promising, detailed measurements were made at this position.

Measurements were made as a series of constant-$\boldsymbol{Q}$ phonon scans at the appropriate positions in reciprocal space to cross the predicted Kikuchi lines for a range of values of $\boldsymbol{k}_s$ (Table 1). Fig. 3 illustrates the phonon scan positions, plotted relative to the [001] and [110] axes. Also shown are predicted k_s Kikuchi line positions for $\boldsymbol{k}_s$ values of $2\cdot90$ and $2\cdot65$ Å^{-1} for $q_\perp > 0$ and $\epsilon = 1$. The intensities of the observed phonon resonances were obtained by fitting a Gaussian on a sloping background to the observed counts in each constant-$\boldsymbol{Q}$ scan. This intensity, corrected for the expected $\boldsymbol{Q}$ variation given

earlier, is plotted as a function of $\boldsymbol{Q}$ in Fig. 6. The calculated Kikuchi line positions are indicated.

5. Results and Discussion

The integrated intensity data for values of k_s ranging from $2\cdot65$ to $2\cdot92$ Å^{-1} are presented in Fig. 6. The positions for the Kikuchi lines derived from Fig. 5 are also shown. There are two general features to be noted in the data. There is the overall decrease in the integrated intensity with decreasing scattered wavevector $\boldsymbol{k}_s$, as a result of the decrease in the volume of reciprocal space sampled due to the reduction in the size of the resolution function. Secondly, there is the variation in the integrated intensity with the wavevector $\boldsymbol{Q}$. It is this latter effect that is of interest in the present investigation.

Referring to Fig. 6 for $k_s = 2\cdot65$ Å^{-1}, there is a marked dip in the integrated intensity centred about $Q_x = 2\cdot1$ ($\sqrt{2}\,2\pi/a$) which is consistent with calculated locations for the unresolved $22\bar{2}$ k_s and k_0 Kikuchi lines. At $k_s = 2\cdot75$ Å^{-1} there is some evidence of increased structure in the Q_x dependence of the integrated intensity that is in accord with the calculated increase in the separation of the $22\bar{2}$ k_s and k_0 Kikuchi lines. However, there is no indication of a variation associated with the predicted locations for the 331 k_s and the $33\bar{1}$ k_0 K-lines.

On increasing $\boldsymbol{k}_s$ further the interpretation of the variations in the integrated intensity becomes much less certain due to the increased number of predicted K-lines in the range of Q_x investigated. Nevertheless, a 20–30% drop in intensity which appears at $Q_x < 2\cdot02$ ($\sqrt{2}\,2\pi/a$) for $k_s = 2\cdot825$ Å^{-1} moves to $Q_x \sim 2\cdot09$ ($\sqrt{2}\,2\pi/a$) at $k_s = 2\cdot92$ Å^{-1}. For $k_s < 2\cdot91$ Å^{-1}, Fig. 5 would indicate that the most likely source of this drop in integrated intensity is the (240, 420) k_0 Kikuchi effect scattering intensity out of the $[1\bar{1}0]$ plane. Although less pronounced, there is also a drop in integrated intensity consistent with the (240, 420) k_0 Kikuchi effect for $Q_x > 2\cdot1$ ($\sqrt{2}\,2\pi/a$) for $k_s = 2\cdot88$ and $2\cdot90$ Å^{-1}. The observed movement of these dips is in accord with that predicted, but the actual values of Q_x for a given value of k_s are too large or too small depending upon whether Q_x is greater or less than $2\cdot1$ ($\sqrt{2}\,2\pi/a$).

Referring to Fig. 4, a drop of ~$0\cdot035$ THz in the calculated frequency would move the (240, 420) k_0 Kikuchi loci into agreement with the observed positions, while only moving the $22\bar{2}$ k_s and k_0 Kikuchi lines a small amount. Furthermore, the (240, 420) lines would then also account for the pronounced double dip observed for $k_s = 2\cdot92$ Å^{-1}.

An examination of the phonon dispersion curves measured at 100 K by Brockhouse *et al.* (1962) indicates that the shift in frequency to correct for dispersion would be of this order. However, our observed phonon frequencies ω which are plotted in Fig. 4 only show evidence of dispersion close to the [001] and [110] directions, with a maximum shift in frequency of ~$0\cdot025$ THz. At the frequencies corresponding to the (240, 420) K-lines the observed frequency shift is negligible.

In addressing the question of the correction to be applied to the observed phonon frequencies we recall that for the Kikuchi effect to be observed the velocity of the neutron must be greater than the velocity of sound in the crystal (Condition 5 in Section 3). This implies that the gradient g of the resolution function in the $(\omega, \boldsymbol{Q}_\perp)$ plane is greater than the slope

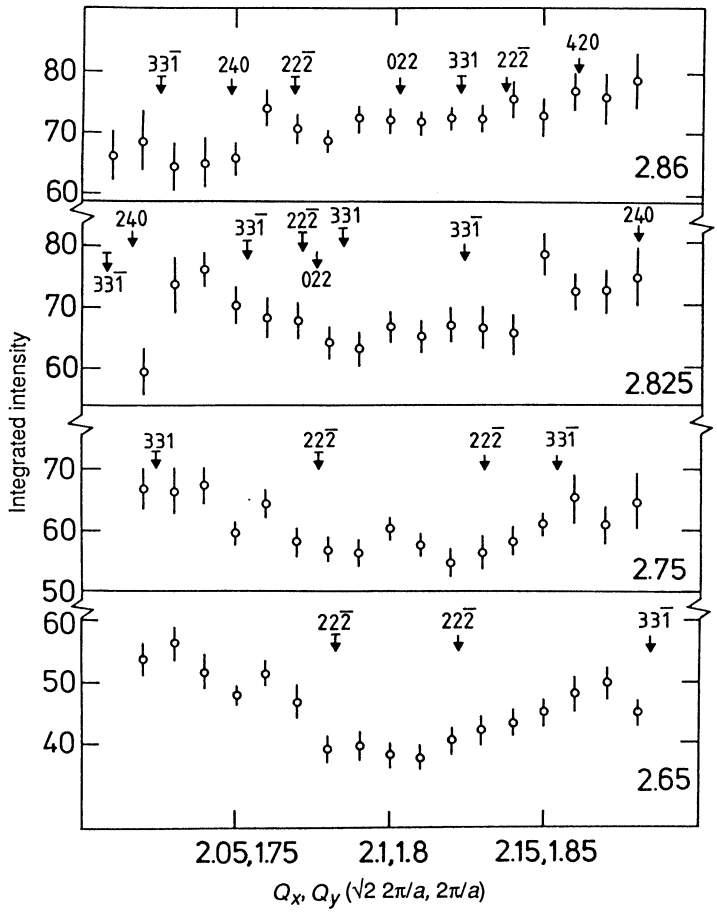

Fig. 6. Variation of integrated intensity of phonons with wavevector $\boldsymbol{Q}$ for (*left*) $k_S = 2\cdot65$, $2\cdot75$, $2\cdot85$ and $2\cdot86\,\text{Å}^{-1}$ and for (*right*) $k_S = 2\cdot88$, $2\cdot90$ and $2\cdot92\,\text{Å}^{-1}$. Arrows with bars indicate the position of k_S lines, those without, k_0 lines.

of the transverse acoustic phonon branch. Thus, the initial (low frequency) part of the resonance will be due to the intersection of the high frequency side of the resolution function with the phonon surface. Conversely, the upper (high frequency) part of the resonance will be due to the intersection of the low frequency side of the resolution function with the phonon surface. At low frequencies the phonon dependent part of equations (6a) and (6b) approximates to a $1/\omega^2$ dependence. Because of this $\sim 1/\omega^2$ factor in the scattering cross section, the intensity for the low frequency side of the resonance is reduced relative to that at the high frequency side, thus shifting the distribution of the resonance to higher frequencies. This is illustrated in Fig. 7.

From Fig. 7 with the approximation of zero frequency spread in the resolution function, the difference between the wavevector $\boldsymbol{q}$ being scanned and that

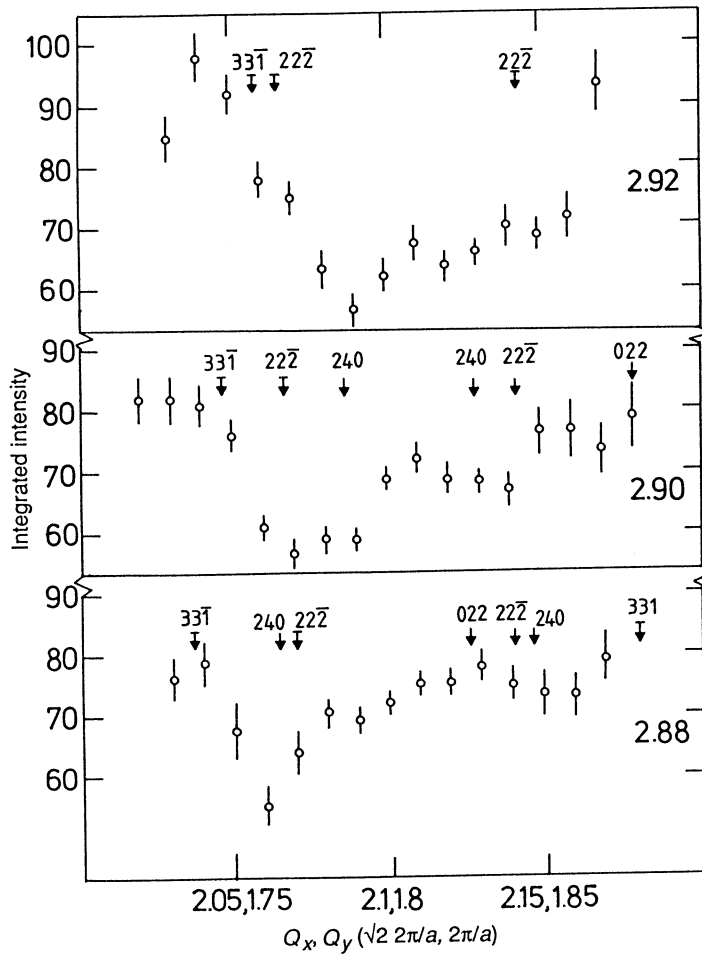

Fig. 6 *(Continued)*

sampled is given by

$$\Delta q = \frac{\omega_{ci} - \omega}{v_s} = \frac{\omega_{ci} - \omega_i}{g}, \tag{7}$$

where ω_i is the frequency corresponding to the point of observation, ω_{ci} is the sampled frequency and ω is the phonon frequency. From equation (7) we get

$$\omega_{ci} = \omega - R(\omega_i - \omega), \tag{8}$$

where $R = (g/v_s - 1)^{-1} = (1/\beta - 1)^{-1}$.

It is implicit in the fitting procedure of the resonance that the $1/\omega^2$ factor is constant, which results in the shift in frequency $\Delta\omega = \omega_f - \omega$ described above, where ω_f is the frequency obtained from the fitted Gaussian peak

$$I_i = I_0 \exp\{-(\omega_i - \omega_f)^2 4 \ln 2/W^2\}, \tag{9}$$

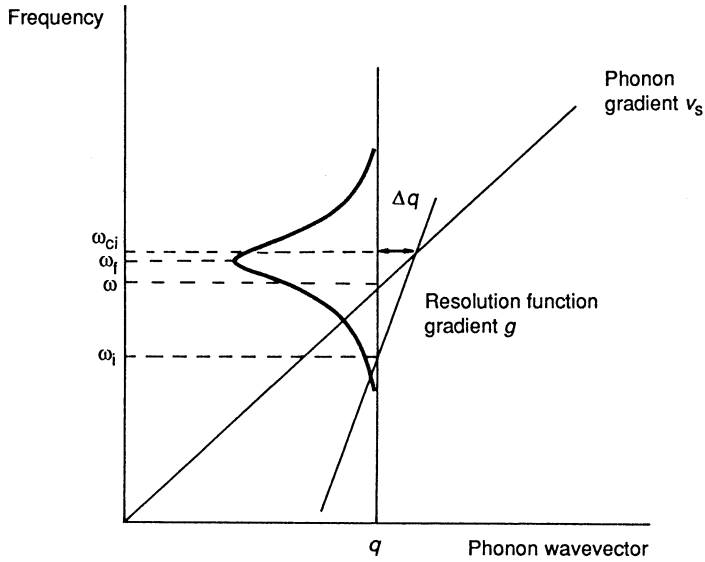

Fig. 7. Schematic representation of the intersection of the resolution function and the phonon surface illustrating the shift in the observed resonance to higher frequencies.

with full width W at $I_0/2$. Thus, the corrected intensity I_{ci} corresponding to ω_{ci} is given by $I_i\,\omega_{ci}^2/\omega_f^2$. The peak shift, $\Delta\omega$ may be estimated from $\Delta I = I_{ci} - I_i$ by using the mean of $\Delta I/\{\partial I_i/\partial(\omega_i - \omega_f)\}$ calculated at each value of $I_0/2$. This leads to the relationship

$$\Delta\omega = \frac{RW^2}{4\omega_f \ln 2}, \tag{10}$$

where R varies from 0·83 to 2·30 for the $\boldsymbol{Q}$ values used in the experiment, with the values of $\Delta\omega$ ranging between 0·01 and 0·03 THz. If the energy resolution is less than that assumed, the shifts will be a bit less than these estimates. These corrections are consistent with the expected dispersion and the shift in frequency required to bring the observations into agreement with the predicted K-lines.

Correcting for dispersion, weak k_s and k_0 Kikuchi lines associated with the $22\bar{2}$ reciprocal lattice point are predicted to occur and move with $\boldsymbol{k}_s$ as observed. Stronger reductions due to the (240, 420) k_0 Kikuchi lines also occur as predicted.

Unfortunately, it has not yet been possible to calculate the relative intensities of the various lines, or explain why the $33\bar{1}$, 331 lines which are also predicted to occur in the range of $\boldsymbol{Q}$ studied (see Fig. 5) were not seen. While further

measurements are required, possibly using a different reciprocal lattice point where fewer K-lines are predicted, the present results are in agreement with the theoretical prediction of the neutron Kikuchi effect.

6. Conclusions

The data presented here provide a reasonable confirmation of the existence of the neutron Kikuchi effect. Analysis of the data was far more complex than originally envisaged and follow-up work on a more exact frequency correction, the effect of the resolution function on the phonon intensities and the relative intensities of the Kikuchi lines themselves is needed. Calculations are in progress to see if other reciprocal lattice points give rise to a less complex pattern of Kikuchi lines, which would thus be simpler to interpret. It also remains for investigations of the effect to be made using different samples, and also to explore whether or not the effect can be observed using a standard four-circle diffractometer.

Acknowledgments

We have benefitted from discussions with a number of people, in particular Drs C. J. Howard, M. S. Lehmann and S. W. Wilkins. We are specifically indebted to Dr C. J. Howard for material used in the Appendix.

Much of this work was carried out at the Lucas Heights Research Laboratories using Australian Nuclear Science and Technology Organisation facilities. The funding for this was made available by the Australian Institute of Nuclear Science and Engineering and the Australian Research Grants Scheme. One of us (S.L.T.) acknowledges support given by a Monash University Scholarship.

References

Born, M., and Huang, K. (1954). 'Dynamical Theory of Crystal Lattices' (Clarendon: Oxford).

Brockhouse, B. N., Arase, T., Caglioti, G., Rao, K. R., and Woods, A. D. B. (1962). *Phys. Rev.* **128**, 1099.

Bushuev, V. A., Laushkin, A. B., Kuz'min, R. N., and Lobanov, N. N. (1983). *Sov. Phys. Solid State* **25**, 228.

Friedrich, W., Knipping, P., and von Laue, M. (1912). *K. Bayer Akad. Munchen Ber.* 302.

Geisler, A. H., Hill, J. K., and Newkirk, J. B. (1948). *J. Appl. Phys.* **19**, 1041.

Graf, H. A., Schneider, J. R., Freund, A. K., and Lehmann, M. S. (1981). *Acta Cryst.* A **37**, 863.

Grenville-Wells, H. J. (1951). *Nature* **168**, 290.

Kashiwase, Y., Kainuma, Y., and Minoura, M. (1982). *J. Phys. Soc. Jpn* **51**, 937.

Kikuchi, S. (1928). *Jap. J. Phys.* **5**, 83.

Petrascheck, D. (1985). *Phys. Rev.* B **31**, 7466.

Ti, S. S., Finlayson, T. R., Smith, T. F., Cashion, J. D., and Clark, P. E. (1983). *Aust. J. Phys.* **36**, 185.

Waldorf, D. L., and Alers, G. A. (1962). *J. Appl. Phys.* **33**, 3266.

Wilkins, S. W. (1983). *Phys. Rev. Lett.* **50**, 1862.

Wilkins, S. W., Chadderton, L. T., and Smith, T. F. (1983). *Acta Cryst.* A **39**, 792.

Appendix

In the reciprocal space formulation presented above, the coordinates for the Kikuchi loci are derived without approximation. This approach is specific to the present experimental investigation. However, to realise the full potential of the Kikuchi effect for self-energy analysis within the sample crystal, requires the detection of K-lines in the standard diffractometer geometry. Thus, the location of K-lines is required in real space $(\Delta 2\theta, \Delta\omega)$ coordinates, where 2θ and ω refer to detector and crystal rotation respectively. It is the purpose of this Appendix to derive the $(\Delta 2\theta^{K}, \Delta\omega^{K})$ coordinates and to demonstrate that these are identical, in the limit that $\Delta 2\theta, \Delta\omega$ are small, to those given previously by Wilkins (1983).

The $q_{\parallel}, q_{\perp}$ axes that were convenient for the derivation of equations (4) are not readily related to $\Delta 2\theta$ and $\Delta\omega$. With a rotation of θ_B^s, the $q_{\parallel}, q_{\perp}$ axes become coincident with the invariant reciprocal space axes q_ω, q_λ. Thus, in matrix form we have

$$\begin{pmatrix} q_\lambda \\ q_\omega \end{pmatrix} = \begin{pmatrix} s' & -c' \\ c' & s' \end{pmatrix} \begin{pmatrix} q_{\parallel} \\ q_{\perp} \end{pmatrix}, \tag{A1}$$

where $s' = \sin\theta_B^s$ and $c' = \cos\theta_B^s$.

The diffractometer coordinates $\Delta 2\theta, \Delta\omega$ are taken to be positive in the anticlockwise sense. Note that this is the reverse of the choice made by Wilkins (1983), but it is in accord with Fig. 1*a* in the present paper, which corresponds to the measurement geometry on the triple-axis spectrometer.

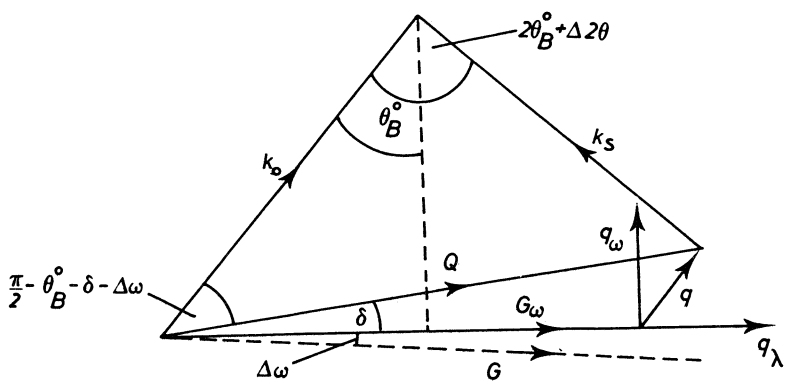

Fig. 8. Scattering geometry for the transformation between $\Delta 2\theta, \Delta\omega$ instrument space and reciprocal space.

The scattering geometry is illustrated in Fig. 8, where

$$\delta = \tan^{-1}\left(\frac{q_\omega}{G + q_\lambda}\right), \qquad Q^2 = (G + q_\lambda)^2 + q_\omega^2. \tag{A2a, 2b}$$

Note that $G_\omega = G$. With $\Delta\omega = 0$, the Bragg condition is satisfied for the incident k_0,

$$G = 2k_0 \sin\theta_B^0. \tag{A3}$$

Applying the cosine rule in the triangle bounded by k_0, k_s and Q gives

$$\cos(2\theta_B^0 + \Delta 2\theta) = \frac{k_0^2 + k_s^2 - Q^2}{2k_0 k_s}, \tag{A4}$$

$$\cos(\pi/2 - \theta_B^0 - \delta - \Delta\omega) = \sin(\theta_B^0 + \delta + \Delta\omega) = \frac{k_0^2 + Q^2 - k_s^2}{2k_0 Q}. \tag{A5}$$

Hence, we get

$$\Delta 2\theta = \cos^{-1}\left(\frac{k_0^2 + k_s^2 - Q^2}{2k_0 k_s}\right) - 2\theta_B^0, \tag{A6a}$$

$$\Delta\omega = \sin^{-1}\left(\frac{k_0^2 + Q^2 - k_s^2}{2k_0 Q}\right) - \theta_B^0 - \delta, \tag{A6b}$$

which are the required values for $\Delta 2\theta$ and $\Delta\omega$.

The theory given previously by Wilkins (1983) was developed using the approximation that $q/k_0 \ll 1$ (we assume that $|k_0 - k_s|/k_0$ is a term of the same order as q/k_0). Retaining only first order terms in q/k_0, equations (A6) can be reduced to

$$(2sck_0)\begin{pmatrix}\Delta 2\theta \\ \Delta\omega\end{pmatrix} = (k_0 - k_s)\begin{pmatrix}2s^2 \\ 1\end{pmatrix} + \begin{pmatrix}2s & 0 \\ s & -c\end{pmatrix}\begin{pmatrix}q_\lambda \\ q_\omega\end{pmatrix}, \tag{A7}$$

where $s = \sin\theta_B^0$. Note that this differs from equation (6) of Wilkins only in the sign of the coefficient of q_ω, this difference being associated with the opposite sense of $\Delta\omega$ with respect to the q_λ, q_ω axes.

The values $q_\parallel^K, q_\perp^K$ corresponding to a point on the Kikuchi locus are given by equations (4), which in the approximation used here are

$$q_\parallel^K = \epsilon\beta q, \qquad q_\perp^K = \pm q(1-\beta^2)^{\frac{1}{2}}, \tag{A8a, 8b}$$

where $\beta = \beta' k_s/k_0$. Furthermore, as $k_0^2 - k_s^2 \approx 2k_0(k_0 - k_s)$ it follows from equation (1) that

$$k_0 - k_s = \epsilon\omega(\boldsymbol{q})\frac{m_n}{\hbar k_0} = \epsilon\beta q. \tag{A9}$$

Using (A1), (A8) and (A9) in (A7) to obtain $\Delta 2\theta^K$ and $\Delta\omega^K$ on the Kikuchi locus gives

$$2csk_0\begin{pmatrix}\Delta 2\theta^K \\ \Delta\omega^K\end{pmatrix} = \begin{pmatrix}2s^2 \\ 1\end{pmatrix}\epsilon\beta q + \begin{pmatrix}2s^2 & -2sc \\ s^2 - c^2 & -2sc\end{pmatrix}\begin{pmatrix}\epsilon\beta q \\ \pm q(1-\beta^2)^{\frac{1}{2}}\end{pmatrix},$$

and hence

$$\Delta 2\theta^{\mathrm{K}} = \{2\epsilon\beta \tan\theta_{\mathrm{B}}^{0} \pm (1-\beta^{2})^{\frac{1}{2}}\} q/k_{0}\,, \tag{A10}$$

$$\Delta \omega^{\mathrm{K}} = \{\epsilon\beta \tan\theta_{\mathrm{B}}^{0} \pm (1-\beta^{2})^{\frac{1}{2}}\} q/k_{0}\,. \tag{A11}$$

Using (A10) and (A11) it is not difficult to show that Wilkins' equation (9) is satisfied. Hence, the theory presented here reduces, near the Bragg condition, to that presented previously by Wilkins.

Manuscript received 23 November 1988, accepted 15 February 1989